

# Suzaku observations of metallicity distribution in the intracluster medium of the NGC 5044 group

Madoka KOMIYAMA<sup>1</sup>, Kosuke SATO<sup>1,2</sup>, Ryo NAGINO<sup>1</sup>, Takaya OHASHI<sup>3</sup>  
and Kyoko MATSUSHITA<sup>1</sup>

<sup>1</sup>*Department of Physics, Tokyo University of Science, 1-3 Kagurazaka, Shinjyuku-ku, Tokyo 162-8601  
j1207629@ed.kagu.tus.ac.jp*

<sup>2</sup>*Graduate School of Natural Science and Technology, Kanazawa University, Kakuma, Kanazawa, Ishikawa 920-1192*

<sup>3</sup>*Department of Physics, Tokyo Metropolitan University, 1-1 Minami-Osawa, Hachioji, Tokyo 192-0397*

(Received 2008 October 31; accepted )

## Abstract

The metallicity distribution in the intracluster medium of the NGC 5044 group was studied up to  $0.3r_{180}$  using the XIS instrument on board the Suzaku satellite. Abundances of O, Mg, Si, S, and Fe were measured with high accuracy. The region within a radius of  $0.05r_{180}$  from the center shows approximately solar abundances of Mg, Si, S, and Fe, while the O/Fe ratio is about 0.5–0.6 in solar units. In the outer region, the Fe abundance gradually drops to 0.3 solar. Radial abundance profiles of Mg, Si and S are similar to that of Fe, while that of O seems to be flatter. At  $r > 0.05r_{180}$ , the mass density profile of O differs from that of Fe, showing a shoulder-like structure that traces the luminosity density profile of galaxies. The mass-to-light ratios for O and Fe in NGC 5044 are one of the largest among groups of galaxies, but they are still smaller than those in rich clusters. These abundance features probably reflect the metal enrichment history of this relaxed group hosting a giant elliptical galaxy in the center.

**Key words:** galaxies:abundances — clusters of galaxies:intracluster medium — groups:individual (NGC 5044 group)

## 1. Introduction

Groups and clusters of galaxies include most galaxies in the nearby universe. (Mulchaey 2000). These systems also represent building blocks of rich clusters and are the best laboratories for the study of thermal and chemical history governed by baryons. An important clue in studying the evolution of galaxies is the abundances of different elements in the hot X-ray emitting gas in groups or clusters of galaxies: namely the intracluster medium (ICM). The metals in the ICM have been synthesized by supernova (SN) in galaxies. As a result, ratios of ICM metal mass to the total light from galaxies in clusters or groups, i.e., metal-mass-to-light ratios, are key parameters in investigating the chemical evolution of the ICM.

Since Fe lines are prominent in X-ray spectra, the content and distribution of Fe in the ICM have been studied in detail. The ASCA satellite first enabled us to measure the distribution of Fe in the ICM (e.g., Fukazawa et al. 2000; Finoguenov et al. 1999). Poor clusters and groups of galaxies exhibit different properties from richer systems in that the derived iron-mass-to light ratios (IMLR) are systematically smaller (Makishima et al. 2001).

Rasmussen & Ponman (2007) reported the temperature and abundance profiles of 15 nearby groups of galaxies observed by Chandra. They showed that Fe abundances of the groups declined from about 1 solar at the center to about 0.1 solar at  $r_{500}$ , which is about  $0.54 r_{180}$ . Si shows less systematic radial variation, indicating SN II contribution increases with radius. Finoguenov et al. (2007) also

reported the metal distributions of groups of galaxies observed by XMM-Newton. They also found that metallicity of some groups drop to 0.1 solar at  $\sim r_{500}$ .

O and Mg are synthesized predominantly in SN II, while Fe and Si are synthesized in both SN Ia and SN II. Abundance measurements spanning the range of species from O to Fe are therefore required for unambiguous determination of the formation history of massive stars. XMM-Newton provided the means to constrain O and Mg abundances in some systems (e.g., Matsushita et al. 2003, Tamura et al. 2003, Matsushita et al. 2007b), however, reliable results have been obtained only for the central regions of very bright clusters or groups of galaxies dominated by cD galaxies.

Suzaku (Mitsuda et al. 2007) is the fifth Japanese X-ray astronomy satellite. The X-ray Imaging Spectrometer (XIS) instrument (Koyama et al. 2007) offers an improved line spread function due to a very small low-pulse-height tail in the energy range below 1 keV coupled with a very low background. Therefore, especially for the regions of low surface brightness or equivalent width, the XIS provides better sensitivity for O lines. The instrumental Al line of the MOS detectors on XMM-Newton causes problems in measuring the Mg abundance in somewhat fainter systems.

With the Suzaku satellite, the oxygen-mass-to-light ratio (OMLR) as well as the IMLR of several clusters of galaxies and several groups of galaxies were measured up to  $0.2\text{--}0.3r_{180}$  (Matsushita et al. 2007a, Tokoi et al. 2008, Sato et al. 2007a, Sato et al. 2008a, Sato et al. 2008b,

Sato et al. 2008c). The OMLR and IMLR increase with the radius, and become relatively flat beyond  $0.1 r_{180}$ . The Fornax cluster, which is the nearest poor cluster with asymmetric X-ray morphology, shows the smallest IMLR and OMLR up to  $0.13 r_{180}$  (Matsushita et al. 2007a).

The NGC 5044 group is a nearby group of galaxies whose redshift is  $z = 0.009020$  from the NASA/IPAC Extragalactic Database (NED). The group has a giant elliptical galaxy NGC 5044 at the center. The X-ray emission of the group shows nearly symmetric spatial distribution (David et al. 1994). The ICM properties in this group have been studied well using XMM-Newton and Chandra by Buote et al. (2003a) and Buote et al. (2003b), and the metal distribution in the outer regions was studied using XMM-Newton (Buote et al. 2004). They revealed that the Fe abundance of the ICM drops from about 1 solar within  $r \approx 50$  kpc to  $\sim 0.4$  solar near  $r \approx 100$  kpc using the solar abundances by Grevesse & Sauval (1998) (Buote et al. 2003b). In the outer region, at  $\sim 176$ – $352$  kpc, the iron abundance is determined to be about 0.15 solar using the same solar abundances (Buote et al. 2004). Tamura et al. (2003) showed O abundance to be 0.25 solar within the central 10–20 kpc using the Reflection Grating Spectrometers (RGS) on XMM-Newton. The mass distribution has been studied using Chandra and ROSAT data (David et al. 1994, Betoya-Nonesca et al. 2006).

We use the Hubble constant  $H_0 = 70$  km/s/Mpc. The distance to the NGC 5044 group is  $D_L = 38.9$  Mpc, and  $1'$  corresponds to  $11.1$  kpc. The virial radius,  $r_{180} = 1.95 (H_0/100)^{-1} \sqrt{k\langle T \rangle / 10 \text{ keV}}$  Mpc (Markevitch et al. 1998, Evrard et al. 1996), is about 880 kpc for the average temperature  $k\langle T \rangle = 1.0$  keV. We use the new abundance table from Lodders et al. (2003) in this paper. Abundances of O and Fe are about 1.7 times and 1.6 times higher than those of Anders & Grevesse (1989), respectively. Unless otherwise specified, errors are quoted at 90% confidence for the single parameter of interest.

## 2. Observations

Suzaku performed three pointing observations of the NGC 5044 group in July 2006. The observational log is shown in Table 1. The first observation (hereafter, the central field) had a pointing direction toward the cD galaxy, NGC 5044. The second and third observations were centered  $15'$  north and  $15'$  east of NGC 5044, respectively (hereafter, the north and east fields, respectively). Figure 1 shows a 0.5–4.0 keV image for the three fields. The observed region covers a distance of about 24 arcmin, or  $\sim 267$  kpc, from NGC 5044.

We also analyzed the MOS and PN data from the XMM-Newton observation of NGC 5044. Details of the data reduction are given in Nagino et al. (2008).

## 3. Spectral Analysis

The XIS was operated in the nominal mode. We included the data formats of both  $5 \times 5$  and  $3 \times 3$  editing modes in our analysis using XSELECT (Ver. 2.3). The

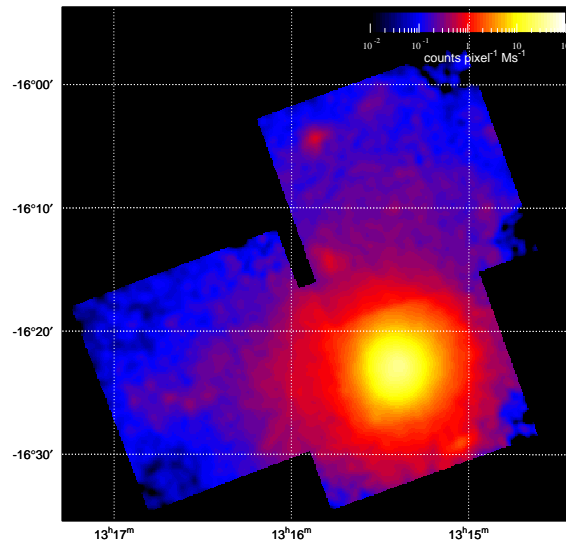


**Fig. 1.** XIS image (0.5–4.0 keV) of the NGC 5044 Group. The NXB (non X-ray background) and CXB (cosmic X-ray background) were subtracted, and the difference in exposure times was corrected. The image was smoothed with a Gaussian of  $\sigma = 16$  pixels.

analysis was performed using HEASoft (Ver. 6.0.6) and XSPEC (Ver. 11.3.2o). After applying the standard data selection criteria, the exposure times of center, north, and east fields were 19.7, 54.6, and 62.4 ks, respectively.

The response of the XRT and XIS was calculated using the `xissimarfgen` ancillary response file (ARF) generator (Ishisaki et al. 2007) and `xismfgen` response matrix file (RMF) generator, version 2006-10-26. Slight degradation of the energy resolution was considered in the RMF, and decrease in the low-energy transmission of the XIS optical blocking filter (OBF) was included in the ARF. The ARF response was calculated assuming a surface brightness profile,  $S(r)$ , based on the analysis of XMM-Newton data by Nagino et al. (2008).

For the central field, we analyzed the spectra extracted from four annular regions of 0–2', 2–4', 4–6', and 6–9' centered on NGC 5044. For the north and east fields, we used the spectra extracted from two annular regions of  $r < 15'$  and  $r > 15'$  centered on the galaxy. Each spectrum was binned to observe details in metal lines, especially O lines. Each spectral bin contained 50 or more counts.

The non X-ray background (NXB) was subtracted from the spectra using the database of night Earth observations with Suzaku for the same detector area and with the same distribution of *COR* (Tawa et al. 2007). We produced the spectra for an energy range 0.4–7.0 keV, since above 7.0 keV, subtraction of background lines is difficult. The spectra of XIS detectors (XIS0, XIS1, XIS2, XIS3) were fitted simultaneously with a model consisting of the ICM emission with additional power-law and the Galactic components.

**Table 1.** Suzaku observations of the NGC 5044 group

Fields	Seq. No.	(RA, Dec) in J2000	Date of obs.	Exp. time
Center	801046010	(13 <sup>h</sup> 15 <sup>m</sup> 24 <sup>s</sup> 0, −16°23′07″8)	2006/07/02	19.7 ks
North	801047010	(13 <sup>h</sup> 15 <sup>m</sup> 24 <sup>s</sup> 0, −16°08′07″8)	2006/07/03	54.6 ks
East	801048010	(13 <sup>h</sup> 16 <sup>m</sup> 26 <sup>s</sup> 5, −16°23′07″8)	2006/07/04	62.4 ks

### 3.1. The ICM component

First, we assumed the ICM consisting of a single temperature *vapec* (Smith et al. 2001) model (hereafter, the 1T model). The metal abundances of He, C, N, and Al were fixed to the solar values. We divided the other metals into seven groups, O; Ne; Mg; Si; S, Ar and Ca; Fe; and Ni, and allowed them to vary. The spectra were subject to a common interstellar absorption,  $N_{\text{H}}$ , fixed at the Galactic values, which are  $5.03 \times 10^{20}$ ,  $4.88 \times 10^{20}$ ,  $5.21 \times 10^{20}$  (atoms/cm<sup>2</sup>) for the center, north, and east fields, respectively.

We also applied a two-temperature (hereafter, 2T) *vapec* model for the ICM, where the metal abundances of the two components were assumed to have the same value.

### 3.2. CXB and discrete sources

The cosmic X-ray background (CXB) was modeled by a power-law spectrum with a photon index  $\Gamma = 1.4$ . The normalization was allowed to vary, which can also account for contributions from discrete sources in galaxies and a possible hard emission.

### 3.3. The Galactic component

The Galactic emission mainly arises from the local hot bubble (LHB) and the Milky-Way halo (MWH). We used two-temperature *apec* thermal spectra for this emission, and by combining it with the 1T model for the ICM we fitted the observed spectra for the outermost ( $r > 15'$ ) regions in the north and east fields. The temperature and normalization of the two components in the Galactic emission were left free with metal abundance fixed to the solar level. The results of the spectral fits are shown in Table 2. The temperature values of the two *apec* models are consistent with the typical values for the LHB and MWH derived by XMM (Lumb et al. 2002).

Since the errors for these temperatures are small, we fixed the temperatures of the LHB and MWH to 0.12 keV and 0.30 keV, respectively. Assuming that the Galactic component has the same surface brightness within the entire observed region, we calculated the normalization of the Galactic component in each region based on the surface brightness measured in the outermost region in the north field. The spectra of the other regions were consistently reproduced with the sum of the ICM model and this Galactic component. This feature supports the view that these *apec* components in the outermost region are dominated by the emission in our Galaxy.

**Table 2.** Temperature of the Galactic components with the 1T model for the ICM.

Region (arcmin/ $r_{180}$ )	$kT_{\text{LHB}}^*$ (keV)	$kT_{\text{MWH}}^*$ (keV)	Ratio of $Norm^{\dagger}$	$\chi^2/\text{d.o.f.}$ -
> 15/0.19 (N)	$0.12^{+0.02}_{-0.01}$	$0.30^{+0.03}_{-0.03}$	$0.48^{+0.21}_{-0.21}$	1113/895
> 15/0.19 (E)	$0.13^{+0.02}_{-0.01}$	$0.29^{+0.07}_{-0.02}$	$0.47^{+0.19}_{-0.23}$	996/895

<sup>†</sup> Ratio of normalization  $Norm_{\text{MWH}}/Norm_{\text{LHB}}$

\* LHB = Local Hot Bubble, MWH = Milky Way Halo

## 4. Results

### 4.1. Fitting results

Table 3 summarizes the best-fit parameters of temperature,  $\chi^2$  values, degrees of freedom, and abundances. For the 2T fitting, the ratios of the *vapec* normalizations and flux between cool and hot ICM components are also summarized in Table 3.

Within  $r = 0.050 r_{180}$ , or  $4'$ , the 2T model significantly improved the fit. For  $0.050 r_{180} < r < 0.19 r_{180}$  ( $4' < r < 15'$ ), the 2T model provided a slightly better fit than the 1T model, while at  $r > 0.19 r_{180}$  ( $15'$ ) the  $\chi^2$  values derived for the 1T and 2T models were nearly equal.

In Figure 2, representative spectra obtained using the XIS-0 and XIS-1 instruments are shown. The spectra are well fitted with the 2T model, and the 1T model provides reasonable fits in the outer region.

### 4.2. Temperature profile of the ICM

We derived the radial temperature profile based on the spectral fit for the annular regions from the group center to  $r \sim 0.3 r_{180}$  (Figure 3a). The fit with the 1T model, within  $r < 0.1 r_{180}$ , showed a temperature increase from 0.8 keV to 1.1 keV. At  $r > 0.2 r_{180}$ , it dropped slightly to 1 keV.

For the 2T model, the temperature of one component showed similar features to that for the 1T fit. Within  $r < 0.1 \sim 0.2 r_{180}$ , we required another component with  $kT \sim 1.5$  keV. The normalization ratio for the cool and hot *vapec* components is shown in Figure 3 (b). The cool component is the strongest in the innermost region. In the outer region, the two components show similar normalizations.

### 4.3. Abundance profiles of the ICM

Radial profiles up to  $r < 0.3 r_{180}$ , or 260 kpc, of abundances of O, Ne, Mg, Si, S, Ar and Ca and Fe are summarized in Table 3 and Figure 4.

On the whole, abundances are high at the center, and decrease toward the outer region. At the center, the 1T

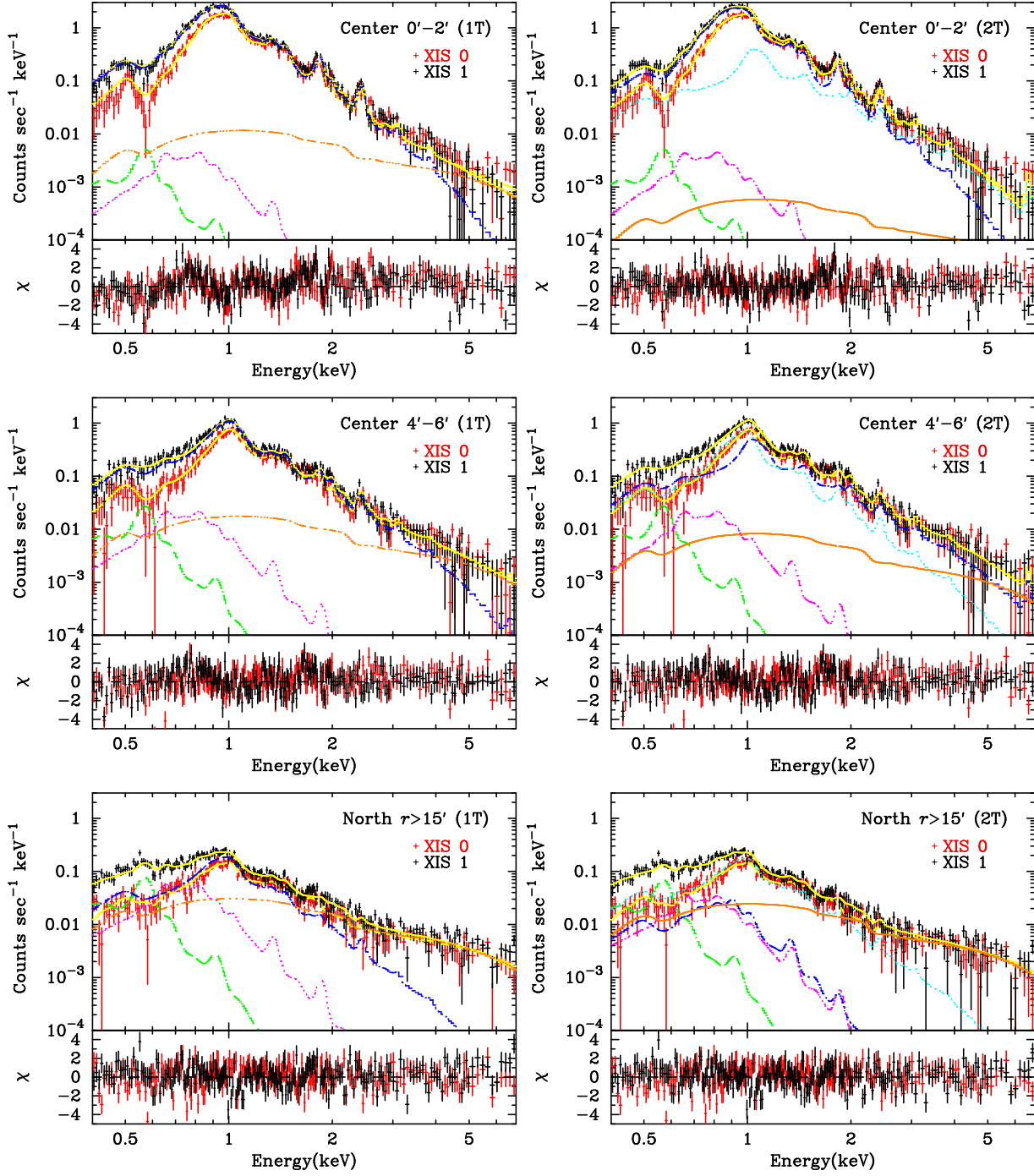


**Fig. 2.** Representative spectra from the XIS-0 (red) and the XIS-1 (black) instruments fitted with the 1T (blue) or 2T (blue and light blue) models for the ICM including the power-law (orange) and the Galactic components (magenta and green). The lower panels show the fit residuals in units of  $\sigma$ .

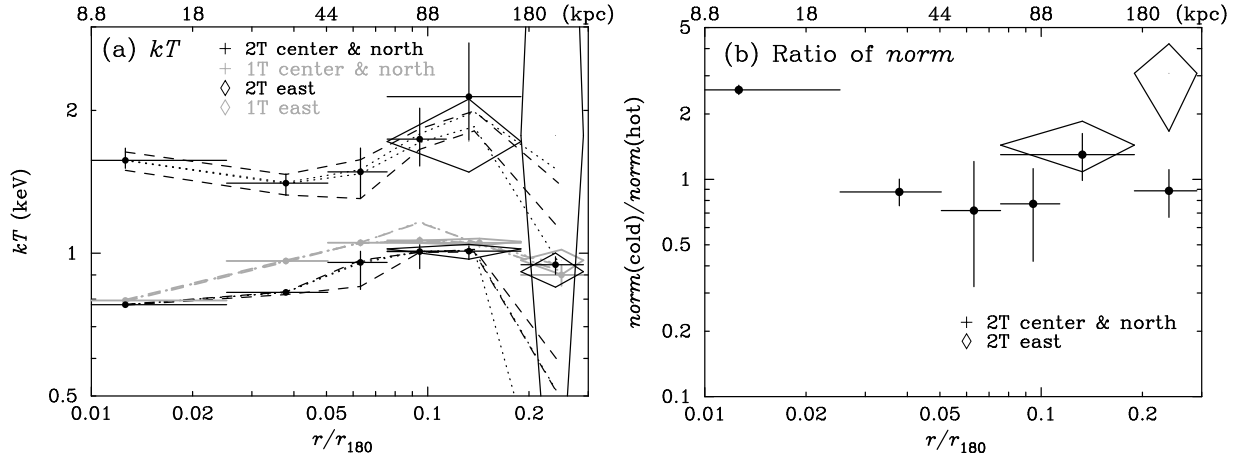


**Fig. 3.** (a) Temperature profile of the ICM derived with the 1T (gray) and the 2T (black) models for the center and the north fields (crosses) and for the east field (diamonds), respectively. Dotted lines indicate shifts of the best-fit values when the NXB level is changed by  $\pm 10\%$ . The dashed lines denote shifts when the thickness of the OBF contaminant is changed by  $\pm 10\%$ . (b) The normalization ratio of the cool and hot components derived from the 2T model fit.

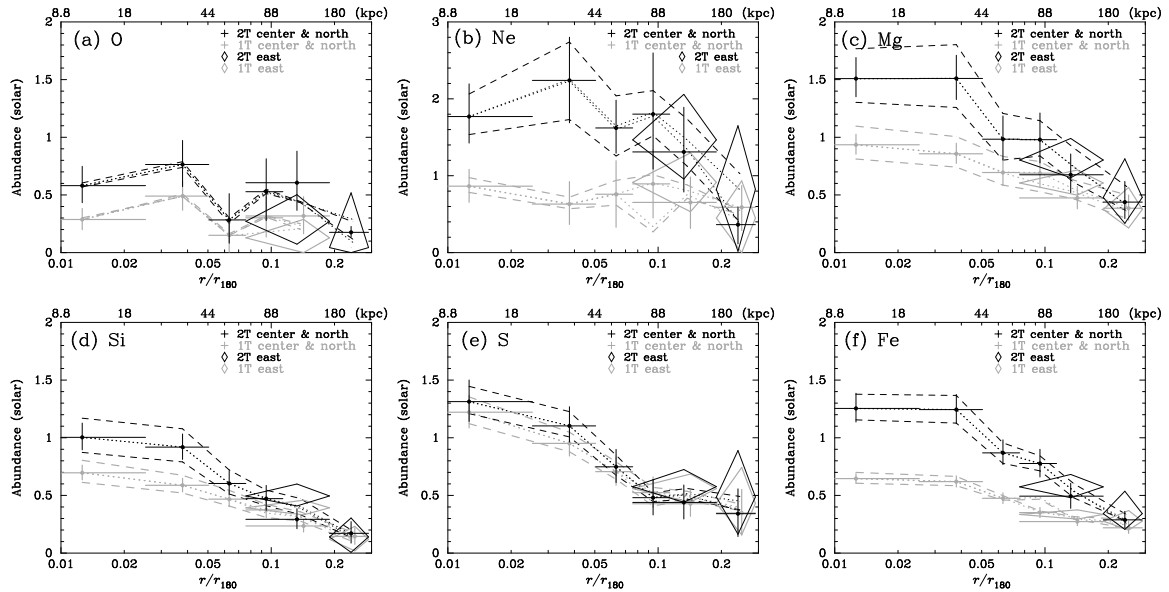


**Fig. 4.** Abundance profiles of (a) O, (b) Ne, (c) Mg, (d) Si, (e) S and (f) Fe of the ICM derived from the 1T (gray) and 2T (black) models for the center and north fields (crosses) and for east field (diamonds), respectively. The dotted lines indicate shifts of the best-fit values when the NXB level is changed by  $\pm 10\%$ . The dashed lines denote shifts when the thickness of the OBF contaminant is changed by  $\pm 10\%$ .

**Table 3.** The ICM temperature,  $\chi^2$ , the ratio of the normalization and abundances of elements derived from the spectral fits for the NGC 5044 group. Errors are in the 90% confidence range of statistical errors, and do not include systematic errors.

Fitting Region (arcmin/ $r_{180}$ )	1T model for the ICM $kT$ (keV)	$\chi^2$ /d.o.f. -	2T model for the ICM $kT_{\text{cool}}$ (keV)	$kT_{\text{hot}}$ (keV)	Ratio of $Norm^\dagger$	Ratio of Flux*	$\chi^2$ /d.o.f. -
0 – 2/0 – 0.025	$0.795^{+0.006}_{-0.006}$	1574/899	$0.779^{+0.007}_{-0.007}$	$1.57^{+0.10}_{-0.06}$	$2.59^{+0.34}_{-0.33}$	3.88	1276/897
2 – 4/0.025 – 0.050	$0.96^{+0.01}_{-0.01}$	1441/899	$0.827^{+0.007}_{-0.008}$	$1.41^{+0.06}_{-0.08}$	$0.88^{+0.11}_{-0.09}$	1.25	1206/897
4 – 6/0.050 – 0.076	$1.05^{+0.01}_{-0.01}$	1194/899	$0.96^{+0.05}_{-0.12}$	$1.48^{+0.18}_{-0.18}$	$0.72^{+0.30}_{-0.26}$	0.90	1123/897
6 – 9/0.076 – 0.11	$1.06^{+0.02}_{-0.02}$	1027/899	$1.01^{+0.03}_{-0.08}$	$1.74^{+0.28}_{-0.21}$	$0.77^{+0.26}_{-0.27}$	0.94	967/897
< 15/0.19 (N)	$1.05^{+0.02}_{-0.02}$	1047/899	$1.01^{+0.03}_{-0.04}$	$2.14^{+0.64}_{-0.41}$	$1.30^{+0.43}_{-0.40}$	1.32	999.5/897
< 15/0.19 (E)	$1.06^{+0.02}_{-0.02}$	963/899	$1.02^{+0.02}_{-0.05}$	$1.72^{+0.39}_{-0.24}$	$1.44^{+0.60}_{-0.51}$	1.61	927/897
> 15/0.19 (N)	$0.90^{+0.04}_{-0.05}$	1091/899	$0.24^{+0.02}_{-0.02}$	$0.95^{+0.04}_{-0.04}$	$0.89^{+0.22}_{-0.22}$	0.27	1112/897
> 15/0.19 (E)	$0.97^{+0.05}_{-0.07}$	970/899	$0.91^{+0.09}_{-0.07}$	$1.77^{+78.13}_{-1.57}$	$3.05^{+3.40}_{-3.05}$	2.95	968/897
1T model for the ICM							
Region (arcmin/ $r_{180}$ )	O (solar)	Ne (solar)	Mg (solar)	Si (solar)	S (solar)	Fe (solar)	Ni (solar)
0 – 2/0 – 0.025	$0.29^{+0.10}_{-0.09}$	$0.86^{+0.22}_{-0.21}$	$0.94^{+0.09}_{-0.08}$	$0.70^{+0.07}_{-0.06}$	$1.22^{+0.15}_{-0.14}$	$0.65^{+0.04}_{-0.04}$	$3.10^{+0.34}_{-0.31}$
2 – 4/0.025 – 0.050	$0.49^{+0.13}_{-0.12}$	$0.63^{+0.29}_{-0.27}$	$0.86^{+0.09}_{-0.08}$	$0.59^{+0.06}_{-0.06}$	$0.95^{+0.12}_{-0.11}$	$0.62^{+0.05}_{-0.05}$	$2.35^{+0.32}_{-0.30}$
4 – 6/0.050 – 0.076	$0.15^{+0.16}_{-0.15}$	$0.76^{+0.44}_{-0.43}$	$0.69^{+0.12}_{-0.11}$	$0.47^{+0.07}_{-0.07}$	$0.71^{+0.13}_{-0.12}$	$0.48^{+0.05}_{-0.05}$	$1.64^{+0.36}_{-0.32}$
6 – 9/0.076 – 0.11	$0.30^{+0.18}_{-0.17}$	$0.89^{+0.44}_{-0.44}$	$0.69^{+0.13}_{-0.12}$	$0.37^{+0.07}_{-0.07}$	$0.52^{+0.14}_{-0.13}$	$0.35^{+0.04}_{-0.04}$	$1.53^{+0.37}_{-0.32}$
< 15/0.19 (N)	$0.32^{+0.17}_{-0.15}$	$0.65^{+0.33}_{-0.34}$	$0.47^{+0.10}_{-0.09}$	$0.24^{+0.06}_{-0.05}$	$0.43^{+0.11}_{-0.11}$	$0.27^{+0.04}_{-0.04}$	$0.98^{+0.28}_{-0.25}$
< 15/0.19 (E)	$0.13^{+0.16}_{-0.13}$	$0.91^{+0.38}_{-0.38}$	$0.60^{+0.11}_{-0.11}$	$0.39^{+0.07}_{-0.06}$	$0.56^{+0.13}_{-0.12}$	$0.34^{+0.04}_{-0.04}$	$1.35^{+0.33}_{-0.29}$
> 15/0.19 (N)	< 0.12	$0.59^{+0.29}_{-0.30}$	$0.38^{+0.11}_{-0.10}$	$0.15^{+0.07}_{-0.07}$	$0.35^{+0.20}_{-0.19}$	$0.22^{+0.06}_{-0.05}$	$0.99^{+0.36}_{-0.35}$
> 15/0.19 (E)	< 0.32	$0.45^{+0.48}_{-0.45}$	$0.37^{+0.19}_{-0.16}$	$0.12^{+0.11}_{-0.10}$	$0.43^{+0.30}_{-0.27}$	$0.28^{+0.09}_{-0.08}$	$0.83^{+0.65}_{-0.55}$
2T model for the ICM							
Region (arcmin/ $r_{180}$ )	O (solar)	Ne (solar)	Mg (solar)	Si (solar)	S (solar)	Fe (solar)	Ni (solar)
0 – 2/0 – 0.025	$0.58^{+0.17}_{-0.15}$	$1.77^{+0.43}_{-0.35}$	$1.51^{+0.18}_{-0.16}$	$1.00^{+0.12}_{-0.11}$	$1.31^{+0.19}_{-0.17}$	$1.25^{+0.13}_{-0.12}$	$2.89^{+0.85}_{-0.68}$
2 – 4/0.025 – 0.050	$0.76^{+0.21}_{-0.19}$	$2.24^{+0.56}_{-0.55}$	$1.51^{+0.20}_{-0.18}$	$0.92^{+0.11}_{-0.11}$	$1.10^{+0.17}_{-0.14}$	$1.24^{+0.13}_{-0.12}$	$1.68^{+0.59}_{-0.51}$
4 – 6/0.050 – 0.076	$0.28^{+0.23}_{-0.20}$	$1.62^{+0.36}_{-0.33}$	$0.98^{+0.20}_{-0.18}$	$0.60^{+0.11}_{-0.10}$	$0.75^{+0.15}_{-0.14}$	$0.87^{+0.11}_{-0.10}$	$1.00^{+0.54}_{-0.46}$
6 – 9/0.076 – 0.11	$0.53^{+0.29}_{-0.25}$	$1.80^{+0.80}_{-0.72}$	$0.98^{+0.23}_{-0.20}$	$0.47^{+0.12}_{-0.10}$	$0.48^{+0.16}_{-0.15}$	$0.78^{+0.12}_{-0.12}$	$0.82^{+0.63}_{-0.53}$
< 15/0.19 (N)	$0.61^{+0.27}_{-0.24}$	$1.31^{+0.58}_{-0.52}$	$0.67^{+0.18}_{-0.15}$	$0.29^{+0.09}_{-0.08}$	$0.44^{+0.15}_{-0.14}$	$0.49^{+0.11}_{-0.11}$	$1.26^{+0.68}_{-0.60}$
< 15/0.19 (E)	$0.27^{+0.23}_{-0.20}$	$1.47^{+0.59}_{-0.51}$	$0.80^{+0.19}_{-0.15}$	$0.50^{+0.10}_{-0.09}$	$0.58^{+0.15}_{-0.14}$	$0.57^{+0.11}_{-0.09}$	$1.30^{+0.61}_{-0.47}$
> 15/0.19 (N)	$0.18^{+0.05}_{-0.04}$	$0.36^{+0.22}_{-0.25}$	$0.44^{+0.18}_{-0.14}$	$0.17^{+0.10}_{-0.08}$	$0.34^{+0.22}_{-0.20}$	$0.29^{+0.07}_{-0.07}$	$0.88^{+0.38}_{-0.44}$
> 15/0.19 (E)	$0.04^{+0.47}_{-0.04}$	$0.82^{+0.83}_{-0.81}$	$0.48^{+0.33}_{-0.22}$	$0.14^{+0.16}_{-0.13}$	$0.49^{+0.40}_{-0.32}$	$0.34^{+0.19}_{-0.14}$	$1.20^{+1.54}_{-0.96}$

\* Ratio of flux in the best fit model  $Flux_{\text{cool}}/Flux_{\text{hot}}$ .† Ratio of normalization  $Norm_{\text{cool}}/Norm_{\text{hot}}$ .

and 2T models give an Fe abundance to be  $\sim 0.7$  solar and  $\sim 1.3$  solar, respectively. These abundances decrease to about 0.3 solar at  $r \sim 0.3 r_{180}$ . In the outer region, the north and east fields give similar Fe abundances suggesting that the metals are mixed over a scale of 100 kpc, or  $\sim 0.1 r_{180}$ .

The abundance profiles of the other elements are shown in Figure 4 (b)-(f). The O profile looks almost flat, although the statistical errors are fairly large. The 1T model fit gives the O abundance to be  $\sim 0.3$  solar, and the 2T model fit gives a two times that value.

The abundance profiles of Mg, Si and S also show negative gradients and resembles the Fe profile. All these abundances drop to about 1/2–1/3 of their central values. The 2T model gives higher Mg and Si abundances in the central regions than the 1T model, while the S abundance shows little dependence on the temperature model. Again, Mg, Si, and S abundances in the north and east

fields are consistent with each other.

The Ne and Ni abundances are significantly higher than those of other elements. Since the K-shell lines of Ne and L-shell lines of Ni are completely mixed with the Fe-L lines, the derived abundances of Ne and Ni might include fairly large systematic uncertainties.

Buote et al. (2004) reported that the Fe abundance is about 0.15 solar at  $0.2\text{--}0.4 r_{\text{vir}}$  using the solar abundances by Grevesse & Sauval (1998), where the solar Fe abundance relative to H is  $3.16 \times 10^{-5}$  by number. In contrast, we have derived about 0.3 solar at  $\sim 0.2\text{--}0.3 r_{180}$  based on the solar abundances of Lodders et al. (2003), where the solar Fe abundance relative to H is  $2.95 \times 10^{-5}$  by number. There is some difference in modeling the background (e.g., the Galactic emission), and the best-fit elemental abundance ratios in our analysis differs from that in Buote et al. (2004). This may cause the discrepancy in the Fe abundances. When the spectra at  $r > 15'$  were fitted with the

1T ICM model without the Galactic emission, we obtained the Fe abundance of 0.1–0.2 solar. However, this model were not able to reproduce the observed spectra at lower energy band, and  $\chi^2$  increased significantly. Another possibility is that at the outer region of  $0.3\text{--}0.4r_{180}$  the Fe abundance might be very much lower than 0.3 solar.

#### 4.4. Profiles of abundance ratios of the ICM

Figure 5 summarizes the abundance ratios of O, Mg, Si, and S divided by the Fe value, all taken in solar units. The abundance ratios, Mg/Fe, and S/Fe, are consistent with the absence of radial gradients. The O/Fe ratio is also consistent with having no radial gradient within rather large error bars. The discrepancies between the 1T and 2T models become much smaller, except for the S/Fe ratio.

The weighted average of the abundance ratios is calculated for the central and offset regions and summarized in Table 4. On average, the abundance ratios are mostly consistent between the center and offset regions. The 2T model indicates O/Fe, Mg/Fe, Si/Fe, and S/Fe abundance ratios to be 0.6, 1.3, 0.7 and 1, respectively. The Ne/Fe ratio might have additional systematic uncertainty due to the overlap with Fe-L lines.

#### 4.5. Uncertainties in the spectral Fits

To estimate the systematic errors, we varied the thickness of the OBF contaminant and the NXB levels by  $\pm 10\%$  in the same manner as in Sato et al. (2008b). The results are summarized in Figure 3 (a) and Figure 4. Here, the values in the north and east offset regions ( $r > 9'$ ) are averaged. Table 5 summarizes  $\chi^2$  values. The 10% decrease in the OBF contaminant gives a slightly better  $\chi^2$  value, while the change in the NXB level has little effect.

We note that the systematic uncertainty in the derived temperature due to the change in the OBF contaminant is less than the statistical error in all the observed regions. In particular, the effect on the cool ICM component is almost negligible. The 10% change in the NXB level gives nearly the same ICM temperature and the effect is insignificant.

The change in the metal abundance due to the 10% change in the OBF contaminant is smaller than 10–20% for all the elements, and it is very close to the statistical error. The change in the NXB level again has a negligible effect on the abundance determination.

In summary, the uncertainty in the NXB level and the OBF contaminant have little effect on the temperature and abundance structures.

#### 4.6. Gas mass profile derived from the XMM-Newton observation

To derive an accurate gas mass profile, we used MOS and PN data from the XMM-Newton observation of NGC 5044. First, to derive accurate normalization for the hot and cool ICM components, we fitted the MOS and PN spectra, which are accumulated within thinner annuli, with the best-fit 2T model derived from the Suzaku spectral fit (3.1). We used the results of the central four annuli of the Suzaku spectra, or within  $\sim 0.11 r_{180}$  (100 kpc). The temperature and abundances of the ICM components

were fixed to the best-fit values derived in Section 4.3, and normalizations of the *vapec* components were left free. To keep the spectral shape of the Galactic and the ICM emission exactly the same as the Suzaku fit, we fixed the normalization ratio for the two components in the Galactic emission, as well as for the two ICM components, in all the annuli.

We then calculated a volume filling factor  $f(r)$  of the cool component (Morita et al. 2006). The fractional volumes of the cool and hot gas,  $V_{\text{cool}}$  and  $V_{\text{hot}}$ , to the total volume  $V$  are given by  $V_{\text{cool}} = fV$  and  $V_{\text{hot}} = (1 - f)V$ , respectively. Because the normalizations of the 2T *vapec* models are expressed as  $Norm_1 = C_{12} n_1^2 V_1$  and  $Norm_2 = C_{12} n_2^2 V_2$  using a certain common constant  $C_{12}$ , the volume filling factor  $f(r)$  can be solved under the pressure balance as (Morita et al. 2006),

$$f(r) = \left[ 1 + \left( \frac{T_{\text{hot}}}{T_{\text{cool}}} \right)^2 \frac{Norm_{\text{hot}}}{Norm_{\text{cool}}} \right]^{-1}. \quad (1)$$

The radial profile of the filling factor is shown in Figure 6 (left), for the XMM and Suzaku data. Considering the difference in the point spread function between the XMM and Suzaku data, the two results of the filling factor agree well. Within  $r < 0.07 r_{180}$ , the cool ICM component is more dominant than in the outer region. This filling factor profile has been fitted with a  $\beta$ -model function,  $f(r) = [1 + (r/r_{c,f})^2]^{-3\beta_f/2}$ , and we obtained  $r_{c,f} = 0.0055 r_{180}$  (4.85 kpc) and  $\beta_f = 0.28$ .

Based on the filling factor result, we derived the gas density distribution in the same way as in Morita et al. (2006) assuming that two temperature components of the ICM exist in the inner part of the extracted regions, or  $r < \sim 0.11 r_{180}$ . In the outer region  $r > \sim 0.11 r_{180}$ , it is not clear whether two ICM components exist. The derived radial profile of electron density  $n_e$  is shown in Figure 6 (right). The best-fit model for the filling factor is significantly smaller than the observed data within  $0.05\text{--}0.2r_{180}$  (Figure 6). However, this discrepancy does not affect the total electron density within several %, since in this region, the electron density of the hot component dominates. Then, we fitted this density profile with a  $\beta$ -model function,  $\rho_{\text{gas}}(r) = \rho_{\text{gas},0} [1 + (r/r_c)^2]^{-3\beta/2}$ , and obtained  $\rho_{\text{gas},0} = 2.4 \times 10^5 (M_\odot/\text{kpc}^3)$ ,  $r_c = 0.032 r_{180}$  (28 kpc) and  $\beta = 0.53$ .

The energy spectra for the XMM-Newton observation were also fitted with the same model as in our 1T fitting (Sec. 3.1). As mentioned above, the single-temperature ICM component was assumed to exist in all extracted regions, or  $r < \sim 0.17 r_{180}$ . The temperature and abundances of the ICM component were fixed to the best-fit values derived in Section 4.3, and normalization of the *vapec* component was left free. We fitted the gas density profile, that was calculated from the normalizations derived from the 1T spectral fit, with a  $\beta$ -model function by fixing  $\beta = 0.51$ , which was obtained from the fitting of the XMM surface brightness profile. The derived parameters of the  $\beta$ -model are  $\rho_{\text{gas},0} = 6.3 \times 10^5 (M_\odot/\text{kpc}^3)$  and

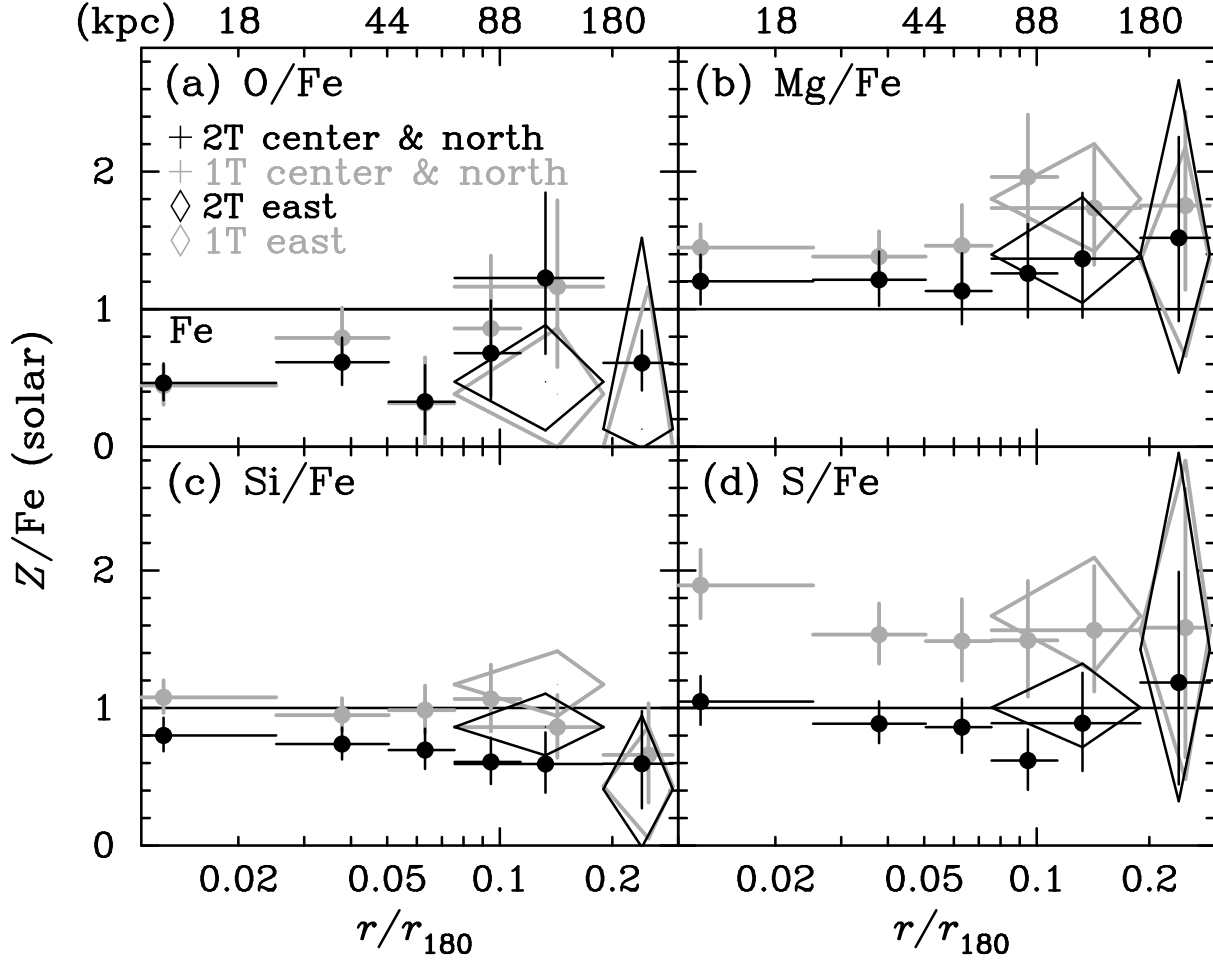


**Fig. 5.** Radial profiles of the abundance ratios of O, Mg, Si, and S divided by the Fe abundance (in units of solar ratio). The meanings of colors and symbols are the same as in Figure 4.

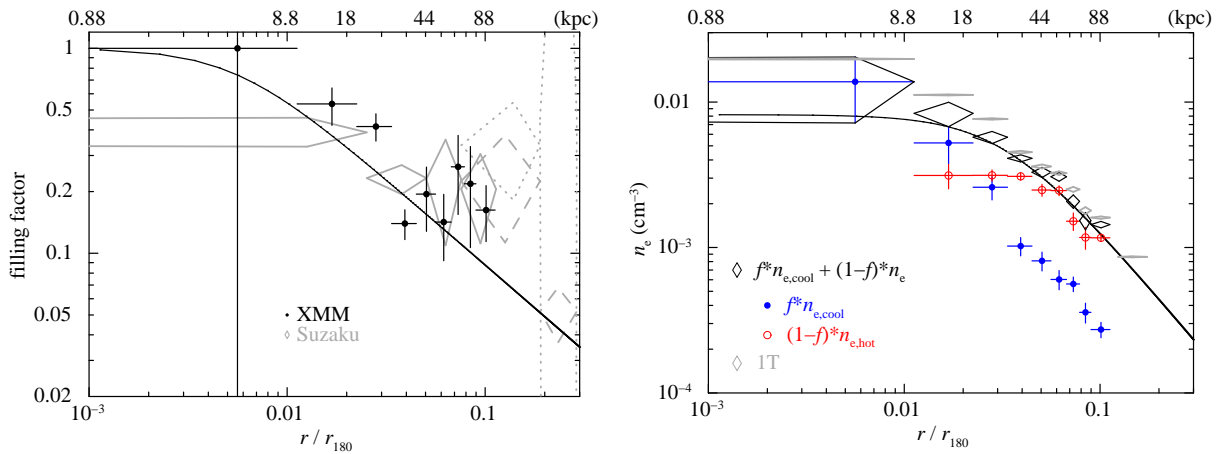


**Fig. 6.** (Left) Filling factor of the cool component derived from XMM (black) and Suzaku (gray), plotted along with the best-fit function of the results from XMM (black solid-line). The Suzaku data for the central four annuli, the north field, and east field are shown in solid, dashed and dotted lines, respectively. (Right) Electron density  $n_e$  ( $\text{cm}^{-3}$ ) obtained using the results of the 1T and 2T fitting. The results for the cool (blue closed circle) and hot (red opened circle) ICM components and the total for the 1T (gray) and 2T (black) models are plotted. The best-fit  $\beta$ -model of the total 2T model is indicated by a solid black line.



**Table 4.** Weighted averages of the abundance ratios in solar units.

Single temperature fitting					
field	O/Fe	Ne/Fe	Mg/Fe	Si/Fe	S/Fe
center	$0.60^{+0.17}_{-0.16}$	$1.62^{+0.43}_{-0.42}$	$1.56^{+0.15}_{-0.14}$	$1.02^{+0.09}_{-0.08}$	$1.60^{+0.16}_{-0.15}$
offset	$0.77^{+0.36}_{-0.35}$	$2.36^{+0.73}_{-0.71}$	$1.66^{+0.31}_{-0.27}$	$0.78^{+0.17}_{-0.15}$	$1.59^{+0.43}_{-0.39}$
all	$0.69^{+0.22}_{-0.19}$	$1.99^{+0.42}_{-0.41}$	$1.61^{+0.17}_{-0.15}$	$0.90^{+0.09}_{-0.09}$	$1.60^{+0.23}_{-0.21}$
Two temperature fitting					
field	O/Fe	Ne/Fe	Mg/Fe	Si/Fe	S/Fe
center	$0.52^{+0.13}_{-0.12}$	$1.85^{+0.33}_{-0.30}$	$1.20^{+0.13}_{-0.12}$	$0.71^{+0.07}_{-0.07}$	$0.85^{+0.10}_{-0.09}$
offset	$0.61^{+0.40}_{-0.17}$	$2.22^{+0.85}_{-0.78}$	$1.42^{+0.40}_{-0.30}$	$0.61^{+0.18}_{-0.15}$	$1.13^{+0.43}_{-0.35}$
all	$0.56^{+0.21}_{-0.10}$	$2.03^{+0.46}_{-0.42}$	$1.31^{+0.21}_{-0.16}$	$0.66^{+0.10}_{-0.08}$	$0.99^{+0.22}_{-0.18}$

**Table 5.** List of  $\chi^2/\text{dof}$  for each fit to study systematic uncertainties

Single temperature fitting					
Region (arcmin/ $r_{180}$ )	Nominal -	Contaminant +10%   -10%		NXB +10%   -10%	
0 – 2/0 – 0.025	1574/899	1685/899	1483/899	1577/899	1571/899
2 – 4/0.025 – 0.050	1441/899	1514/899	1389/899	1447/899	1436/899
4 – 6/0.050 – 0.076	1194/899	1239/899	1160/899	1203/899	1187/899
6 – 9/0.076 – 0.11	1027/899	1055/899	998/899	1030/899	1019/899
< 15/0.19 (N)	1047/899	1068/899	1034/899	1070/899	1036/899
< 15/0.19 (E)	963/899	999/899	937/899	990/899	949/899
> 15/0.19 (N)	1091/899	1095/899	1094/899	1100/899	1095/899
> 15/0.19 (E)	969/899	983/899	965/899	994/899	964/899
Two temperature fitting					
Region (arcmin/ $r_{180}$ )	Nominal -	Contaminant +10%   -10%		NXB +10%   -10%	
0 – 2/0 – 0.025	1276/897	1317/897	1245/897	1277/897	1275/897
2 – 4/0.025 – 0.050	1206/897	1239/897	1183/897	1209/897	1204/897
4 – 6/0.050 – 0.076	1122/897	1148/897	1105/897	1129/897	1118/897
6 – 9/0.076 – 0.11	967/897	981/897	957/897	973/897	964/897
< 15/0.19 (N)	999/897	1001/897	1002/897	1008/897	999/897
< 15/0.19 (E)	927/897	946/897	915/897	943/897	921/897
> 15/0.19 (N)	1111/897	1099/897	1117/897	1109/897	1115/897
> 15/0.19 (E)	967/897	975/897	965/897	986/897	964/897

$r_c = 0.017 r_{180}$  (15 kpc).

By integrating the gas density  $\rho_{\text{gas}}$ , we derived the integrated gas mass profile for the 1T and 2T models (Figure 7). For the 2T model, the sum of the cool and hot components is plotted. At  $r > 0.11 r_{180}$  for the 2T fit and  $r > 0.17 r_{180}$  for the 1T fit, we extrapolated the gas mass profile using the best-fit  $\beta$  model. A clear difference in the gas mass profile between the 1T and 2T models is seen in the central region,  $r < \sim 0.03 r_{180}$ , while at  $r > \sim 0.03 r_{180}$ , the two models give similar gas mass profiles. Within  $2'$  from the center, the temperatures of the ICM derived from the 1T model and from the cool component of the 2T model, which contributes most of the Fe-L emission, are nearly the same. In contrast, the 1T model gives a lower Fe abundance than the 2T case. To reproduce similar intensity in the Fe-L band, a higher gas mass is required for the 1T model.

The gas mass profile derived from ROSAT observation (David et al. 1994) is also shown in Figure 7. The ra-

dial gradient of our gas mass profile agrees well with the ROSAT result, while the absolute values are larger than the ROSAT level by several tens of percentages, which is probably due to different assumptions about the metal abundance.

Integrated and differential mass profiles of O, Mg, and Fe were derived from the gas mass and abundance profiles (Figure 7). In contrast to the gas mass profile, the metal mass profiles derived from the 1T and 2T models agree well in the central region. Hereafter, we use the metal mass profiles derived from the 2T model.

## 5. Discussion

### 5.1. The Fe abundance profiles of the ICM

The radial profile of Fe abundance in the NGC 5044 group is compared with those in other groups, HCG 62 (Tokoi et al. 2008), the NGC 507 group (Sato et al. 2008b), and the Fornax cluster (Matsushita et al. 2007a) observed with Suzaku (Figure 8). The three groups show similar

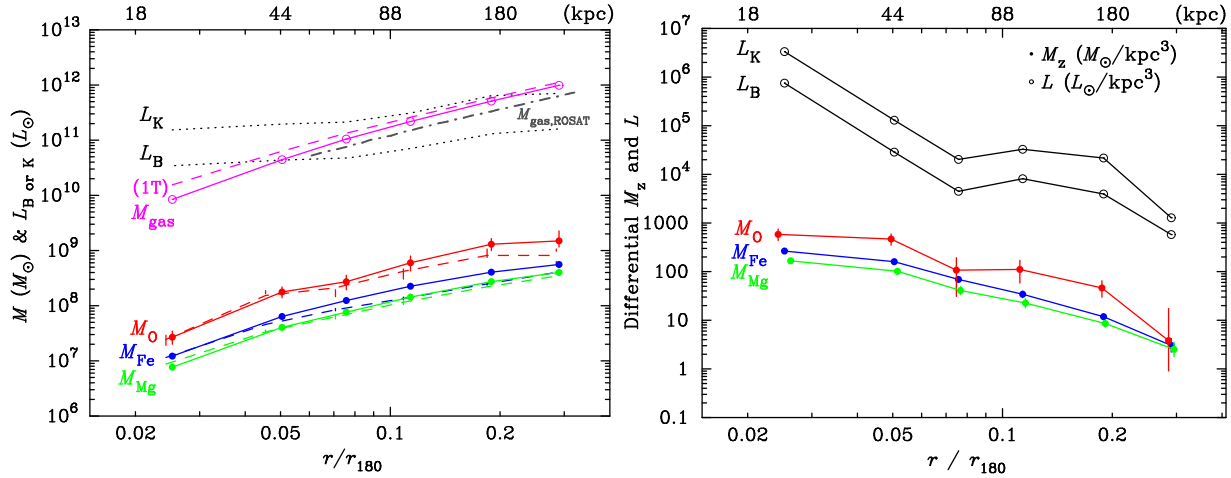


**Fig. 7.** (Left) Integrated mass of the hot gas (magenta), and those of O (red), Fe (blue), and Mg (green). Integrated B-band and K-band luminosities of galaxies,  $L_B$  and  $L_K$  (dotted lines), are also plotted. The dashed and solid lines correspond to the mass derived from the 1T and 2T model fit, respectively. The gray dot-dashed line shows the gas mass derived using ROSAT (David et al. 1994). (Right) Differential metal mass density profiles (blue, red and green solid lines) derived for the 2T model and luminosity density profiles of  $L_B$ , and  $L_K$ .

Fe abundance profiles. The Fe abundance is 1.2–1.5 solar at the center, and gradually decreases to 0.5 solar at  $0.1r_{180}$ . The value of 0.5 solar is close to the level observed in general clusters of galaxies at  $0.1\text{--}0.3r_{180}$  (Matsushita 2008). These groups are characterized by nearly symmetric X-ray morphology with a bright central galaxy, and the enhanced Fe abundance within  $0.1r_{180}$  should reflect Fe accumulation in the central galaxies over a long time. The NGC 5044 group shows similar Fe abundance in the north and east fields, suggesting that the group gas has evolved by keeping global spatial symmetry. In contrast, the Fornax cluster shows nearly constant Fe abundance at 0.5 solar over a radial range of  $0.02\text{--}0.13r_{180}$  from the cD galaxy, NGC 1399. This cluster has asymmetric X-ray morphology, and NGC 1399 is significantly offset from the center (Paolillo et al. 2002, Scharf et al. 2005). Chandra observations suggest that NGC 1399 may be relatively moving against the ICM (Scharf et al. 2005). Therefore, around NGC 1399, a recent supply of metals from the cD galaxy produces a sharp peak of Fe abundance within  $0.02r_{180}$ .

### 5.2. The abundance pattern of the ICM and contributions from SN Ia and SN II

Figure 9 summarizes the abundance pattern for O, Mg, Si, S and Fe in four systems: the NGC 5044 group, HCG 62, the NGC 507 group and the Fornax cluster. The derived ratios, O/Fe, Mg/Fe, Si/Fe and S/Fe, all scatter around unity, i.e., the solar ratio. The four systems show similar Si/Fe and S/Fe ratios. The NGC 5044 group shows the smallest O/Fe ratio, 0.6, compared with  $\sim 0.8$  in the other three systems. In contrast, the NGC 5044 group shows the highest Mg/Fe ratio of 1.2 among the four systems derived from the 2T model. The 2T and 1T models give different abundance ratios by a few tens of percentages. The uncertainty due to coupling with the Fe-L lines

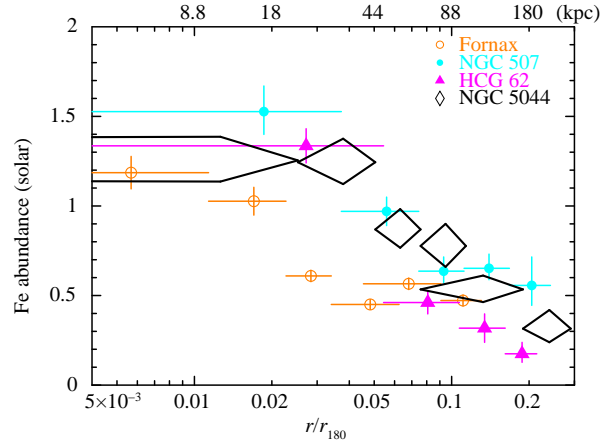


**Fig. 8.** Radial profiles of the Fe abundance in the NGC 5044 group (diamonds), the Fornax cluster (Matsushita et al. 2007a, open circles), the NGC 507 group (Sato et al. 2008b, closed circles), and HCG 62 (Tokoi et al. 2008, closed triangles).

may result in a 20–30% systematic error in the Mg abundance (Matsushita et al. 2007a), and the estimation of the Galactic emission leaves some uncertainty in the O abundance. Considering the systematic uncertainty mentioned here, the abundance pattern for O, Mg, Si, S, and Fe does not differ significantly among the four poor systems.

As shown by Sato et al. (2007b), the abundance pattern of the NGC 5044 ICM within  $0.1r_{180}$  and  $0.1\text{--}0.3r_{180}$  can be fit by a combination of average SNe Ia and SNe II yields (Figure 10). The SNe Ia and II yields were taken from Iwamoto et al. (1999) and Nomoto et al. (2006), respectively. About 80% of Fe and  $\sim 40\%$  of Si and S in the ICM are synthesized by SN Ia. The derived number ratio of SNe II to SNe Ia is  $3.1 \pm 0.6$  and  $3.3 \pm 0.7$ , for  $r < 0.1r_{180}$  and  $0.1r_{180} < r < 0.3r_{180}$ , respectively, assuming

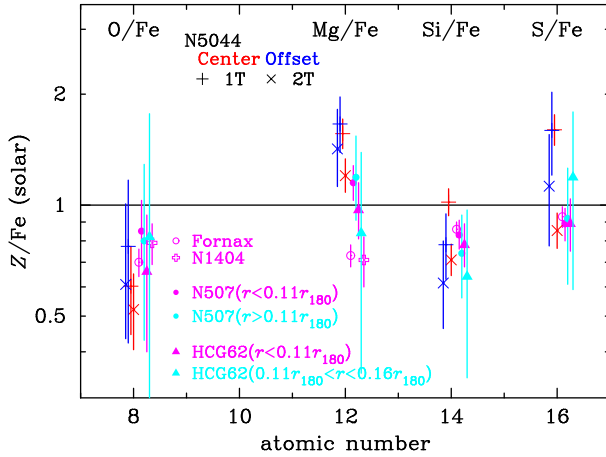


**Fig. 9.** Weighted averages of the abundance ratios of various elemental species compared to Fe for the central (red;  $r < \sim 0.1r_{180}$ ) and offset (blue;  $r > \sim 0.1r_{180}$ ) fields of the NGC 5044 group. Those in the regions within  $\sim 0.1r_{180}$  (magenta) and  $0.1 \sim 0.3r_{180}$  (light blue) of the NGC 507 group (Sato et al. 2008b), HCG 62 (Tokoi et al. 2008), the Fornax cluster (Matsushita et al. 2007a), and an elliptical galaxy NGC 1404 (Matsushita et al. 2007a) are also plotted.

a classical deflagration model, W7, for SNe Ia. This is close to the value of 3–4, obtained for the other groups of galaxies, NGC 507 and HCG 62, and several other clusters of galaxies (Sato et al. 2007b).

When systems have a similar initial mass function of stars (IMF) and are old enough, most SN Ia and SN II would have already exploded. To explain abundance pattern of stars in the solar neighborhood, lifetimes of SN Ia are confined within 0.5–3 Gyr, with typical lifetime of 1.5 Gyr (Yoshii et al. 1996). In clusters of galaxies, to account for Fe mass in the ICM, the past average rate of SNe Ia was much larger than the present rate in elliptical galaxies (e.g., Renzini et al. 1993). This result indicates that lifetimes of most of SN Ia are much shorter than the Hubble time. In this case, the final abundance pattern should be similar. If the IMF is close to that in our Galaxy and most of stars in our Galaxy and clusters were already formed before a few Gyrs ago, the abundance pattern should naturally be similar to the solar abundance pattern. Within  $0.1r_{180}$  of NGC 5044, the gas mass and stellar mass are pretty close (§5.3). The mean stellar metallicity and  $[\alpha/\text{Fe}]$  derived from optical observations are about 1 solar and  $0.34 \pm 0.17$ , respectively (Kobayashi & Arimoto 1999, Annibali et al. 2007). Therefore, the sum of the low O/Fe ratio found in the ICM and the high stellar  $\alpha/\text{Fe}$  values may give roughly the solar abundance pattern. However, in this study, we are combining the abundances of two distinct bodies, stars and ISM, which may have very different enrichment histories.

### 5.3. The radial profiles of the metal mass-to-light ratios

Since metals in the ICM are all synthesized in galaxies, the metal-mass-to-light ratio is a useful measure for the study of ICM chemical evolution. To estimate the metal mass-to-light ratio, we calculated B-band and K-band lu-

minosity profiles. Ferguson & Sandage (1990) (hereafter, FS90) have optically studied the NGC 5044 group, and identified 162 member galaxies whose apparent magnitudes,  $m_B$ , are brighter than  $m_B \sim 20$ , with a completeness limit of  $m_B \sim 18$ . They also show that the central elliptical galaxy NGC 5044 has an apparent magnitude of  $m_B = 11.9$ , or  $\log L_B/L_{B,\odot} = 10.7$  using the luminosity distance  $D_L = 38.9$  Mpc and the foreground Galactic extinction  $A_B = 0.300$  (Schlegel et al. 1998) from NED. Since this galaxy dominates the central region, we applied the de Vaucouleurs' law to calculate the luminosity profile within  $0.076 r_{180}$  ( $6'$ ), and deprojected the profile using the expression by Mellier & Mathez (1987). In the outer region,  $r > 0.076 r_{180}$ , we integrated the luminosities of the member galaxies from FS90 and deprojected the profile.

Since the K-band luminosity of a galaxy correlates well with the stellar mass, we also collected K-band magnitudes of galaxies in a box of  $2 \times 2 \text{ deg}^2$  centered on NGC 5044 from the Two Micron All Sky Survey (2MASS). NGC 5044 itself has an apparent magnitude  $m_K = 7.845$ , or  $\log L_K/L_{K,\odot} = 11.4$  using the foreground Galactic extinction  $A_K = 0.026$  (Schlegel et al. 1998) from NED. The average surface brightness in the region of  $r > r_{180} = 79.2'$ ,  $L_{K,\text{bgd}} = 3.01 \times 10^9 L_{K,\odot}$ , is subtracted as the background. We then calculated the K-band luminosity profile in the same way as for the B-band profile.

Forty-three objects are detected in both the B-band and K-band (Figure 11). As shown in Figure 11, the two magnitudes of these objects correlate well with each other.

The integrated B-band and K-band luminosity profiles are shown in the left panel of Figure 7 and in Figure 12. The two band profiles resemble each other; the ratio of the integrated luminosity,  $L_B/L_K$ , is nearly constant at  $\sim 0.22$  (figure 12). This corresponds to  $B - K \sim 4.1$ , which is consistent with  $B - K = 4.2$  for early-type galaxies in Lin & Mohr (2004). The NGC 5044 galaxy dominates the luminosity profile in the region  $r < \sim 0.07 r_{180}$ , while in the outer region,  $r > \sim 0.07 r_{180}$ , the contribution from fainter galaxies in the group becomes important.

The luminosity density profiles of  $L_B$  and  $L_K$  are plotted in the right panel of Figure 7. These profiles are compared with the mass density profiles of O, Mg and Fe from the 2T model fit. We note that the mass densities of stars and O both indicate a shoulder-like structure in the region from  $0.06r_{180}$  to  $0.2r_{180}$ . The profiles of Mg and Fe do not show such a shoulder and decrease smoothly. Therefore, the oxygen distribution seems to closely correlate with that of small galaxies in the group.

The integrated mass-to-light ratios for O, Mg and Fe (OMLR, MMLR and IMLR) using B-band and K-band luminosities are summarized in Table 6 and Figure 13 (left). The error bars of the mass-to-light ratios include only the abundance errors. The profiles increase with the radius up to  $r \sim 0.1 r_{180}$ , in the region where NGC 5044 dominates, and then become almost constant in the outer region.

Our IMLR value with the B-band luminosity is  $\sim 3.6 \times 10^{-3}$  expressed in terms of solar values at  $r < 0.3 r_{180}$ . This value is consistent with the result of Buote et al.

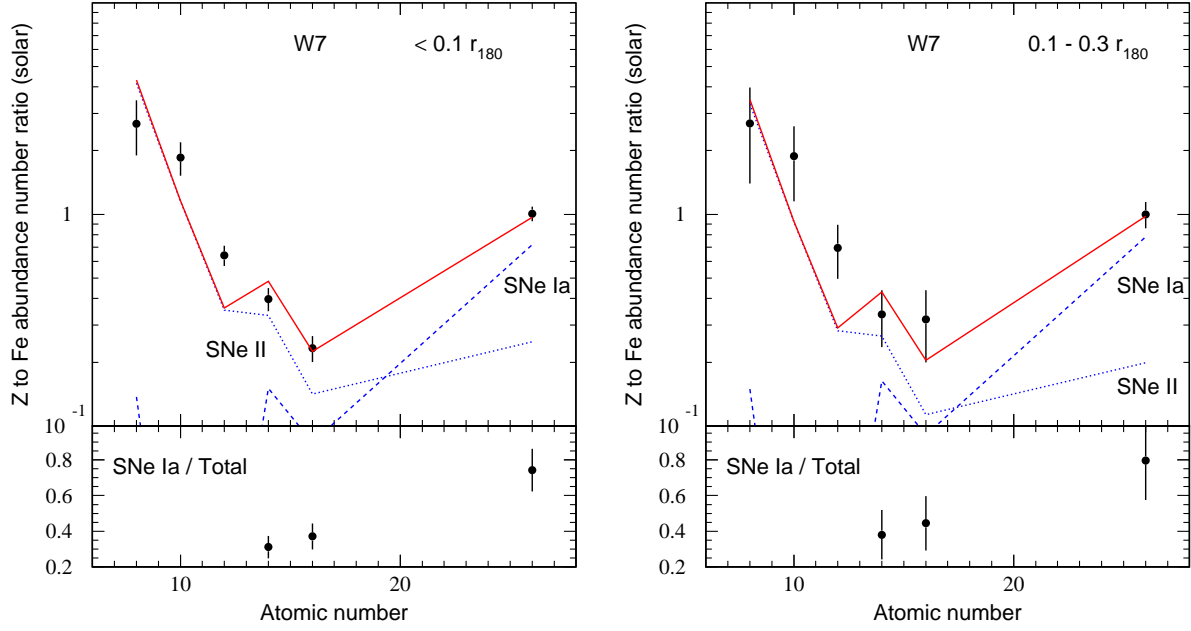


**Fig. 10.** Fit results of number ratios of elements to Fe of the NGC 5044 group within  $0.1 r_{180}$  (**left**) and  $0.1-0.3 r_{180}$  (**right**). Top panel shows the number ratios (closed circles). Blue dashed and dotted lines correspond to the contributions of SNe Ia (W7) and SNe II, respectively, and the red line corresponds to the sum of the two. Ne (atomic number = 10) is excluded from the fit. The bottom panel indicates fractions of the SNe Ia contribution to total mass in the best-fit model for each element.

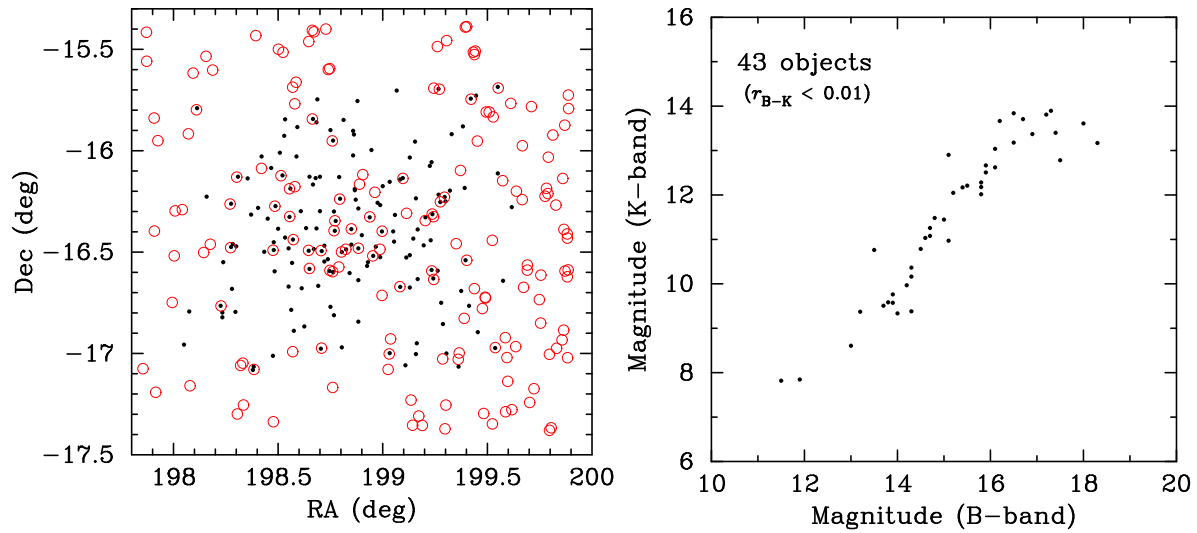


**Fig. 11.** (**Left**) Objects detected in B-band and K-band (black closed circle: B-band, red open circle: K-band). (**Right**) Correlation of magnitude of B-band and K-band for objects detected in both bands.

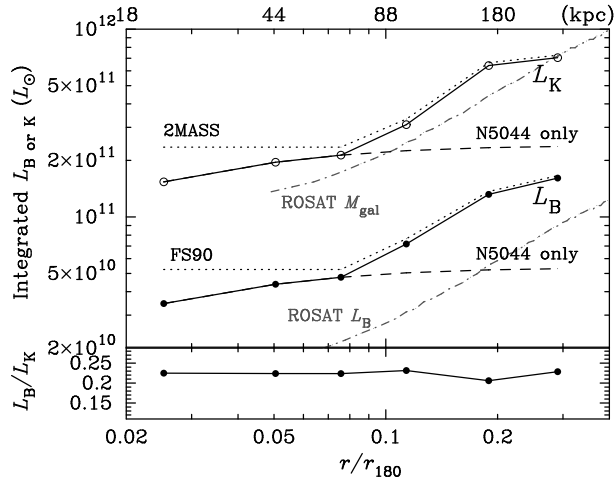


**Fig. 12.** Integrated luminosity profiles in B-band and K-band. The dashed lines indicate luminosity of the central galaxy NGC 5044.

(2004), since our larger derived Fe abundance gives a smaller gas mass.

We also calculated differential metal-mass-to-light ratios, as shown in the right panel of Figure 13. The differential OMLR becomes almost flat in the region  $r > \sim 0.07 r_{180}$ , while IMLR and MMLR show a clear drop in  $0.1-0.2 r_{180}$  compared with the level at  $0.07 r_{180}$ . In other words, the O distribution seems to be more extended than those of Fe and Mg, although the error in the data is fairly large. There may be some difference in the metal production process between the giant elliptical galaxy, NGC 5044, and smaller galaxies, in connection with a different history of SN Ia and SN II activity.

#### 5.4. Comparison of the metal-mass-to-light ratios with other systems

The metal-mass-to-light ratios of the NGC 5044 group are compared with those in other groups and clusters. The objects are, the NGC 507 group and HCG 62, the Fornax cluster as a poor cluster, and other clusters of galaxies with ICM temperatures of 2–4 keV: A 262, A 1060, AWM7, and the Centaurus cluster, as summarized in Figure 14 and Table 7. The gas mass of these systems were derived using XMM-Newton data except the Fornax cluster, where the ROSAT data was used.

The OMLR, MMLR, and IMLR for clusters of galaxies with  $kT \sim 2-4$  keV tend to be higher than those in groups of galaxies and the poor cluster of galaxies with  $kT \sim 1$  keV. However, the data points might have some systematic uncertainty, possibly because of different observations of B-band luminosity of galaxies, statistics in the number counts of galaxies, and systematic shift of gas mass derived from XMM observations with different sensitivities and fields of view.

The difference in the OMLR values between groups and clusters is about a factor of 3–6, and systematically larger than the IMLR and MMLR difference, which is a factor of 2–3. Among groups, the NGC 5044 group and HCG 62

have the highest IMLRs, which are comparable to those of clusters. In contrast, OMLR of the NGC 5044 appears to be lower than those of clusters. Among the groups and poor clusters, the Fornax cluster shows the lowest IMLR and OMLR. In the Fornax cluster, the asymmetric X-ray emission may point to large-scale dynamical evolution, which might have hampered the strong concentration of hot gas in the center.

These poor systems also differ from richer systems in that the gas density profile in the central region is significantly flatter and the relative entropy level is correspondingly higher (e.g. Ponman et al. 1999). These peculiar central characteristics in the poor systems are thought to be best attributed to an injection of energy (preheating) into the gas before clusters have collapsed (e.g. Kaiser 1991). Note also that more recent observations and simulations of entropy profiles indicate some modification to this simple picture (e.g. Ponman et al. 2003).

Metal distribution in the ICM can be a powerful tracer of the history of such a gas heating in the early epoch, since the relative timing of metal enrichment and heating should affect the present amount and distribution of metals in the ICM. To look into this, we assume that all galaxies synthesize a similar amount of metals per unit stellar mass. If metal enrichment occurred before the energy injection, the poor systems would carry relatively smaller metal mass with smaller gas mass than those in rich clusters, while metal abundance would be quite similar to those in rich clusters. In contrast, if metal enrichment occurred after the energy injection, the metal mass becomes comparable to those in rich clusters and indicates a higher abundance. The difference in O and Fe distributions would constrain the timing of energy injection, since O was synthesized by SN II during galaxy star formation, while Fe was mainly produced by SN Ia much later than this period.

The OMLR shows a larger difference in clusters and groups than the IMLR does, which may reflect the condition that SN II products are more extended in groups due to the effect of preheating. Fe was synthesized later by SN Ia, and may be irrelevant to preheating. To further investigate the problem of heating and enrichment, we need numerical simulations including the effect of the preheating and metal enrichment by both SN II and SN Ia.

## 6. Summary and Conclusion

Suzaku observations of the NGC 5044 group, with a relatively symmetric X-ray morphology, allowed determination of the abundances of O, Mg, Si, S and Fe in the ICM up to  $0.3 r_{180}$  fairly accurately. The Fe abundance around NGC 5044 is about a solar and drops to 0.3 solar at  $0.3 r_{180}$ . The abundance ratios, Mg/Fe, Si/Fe and S/Fe, are close to the solar ratio, while O/Fe is 0.5–0.6 in solar units. The abundance pattern indicates that most of the Fe should have been synthesized by SN Ia. The O distribution closely resembles the light distribution of galaxies, in particular in the outer region. The OMLR of the NGC

**Table 6.** Summary of metal-mass-to-light ratios of NGC 5044

B-band							
$r$ ( $r_{180}$ )	$r$ (arcmin)	$r$ (kpc)	$L_B$ $10^{10} L_\odot$	$M_{\text{gas}}$ $10^{11} M_\odot$	IMLR	OMLR	MMLR
					$\times 10^{-3} (M_\odot/L_\odot)$		
0.025	2	22	3.5	0.084	$0.35^{+0.04}_{-0.03}$	$0.78^{+0.22}_{-0.20}$	$0.22^{+0.03}_{-0.02}$
0.050	4	44	4.4	0.44	$1.5^{+0.1}_{-0.1}$	$4.1^{+1.0}_{-0.9}$	$0.92^{+0.10}_{-0.09}$
0.076	6	66	4.8	1.0	$2.6^{+0.2}_{-0.2}$	$5.7^{+1.8}_{-1.6}$	$1.6^{+0.2}_{-0.2}$
0.11	9	100	7.2	2.2	$3.1^{+0.3}_{-0.2}$	$8.3^{+2.7}_{-2.4}$	$2.0^{+0.3}_{-0.2}$
0.19	15	167	13	5.1	$3.1^{+0.2}_{-0.2}$	$9.9^{+2.6}_{-2.3}$	$2.1^{+0.2}_{-0.2}$
0.29	23	256	16	9.9	$3.5^{+0.4}_{-0.3}$	$9.3^{+4.8}_{-2.1}$	$2.5^{+0.4}_{-0.3}$
0.10*	7.9	88	7.2	1.7	$2.6^{+0.2}_{-0.2}$	$6.6^{+1.9}_{-1.7}$	$1.6^{+0.2}_{-0.2}$
0.30*	24	264	16	1.0	$3.6^{+0.4}_{-0.3}$	$9.4^{+5.2}_{-2.1}$	$2.6^{+0.4}_{-0.3}$
K-band							
$r$ ( $r_{180}$ )	$r$ (arcmin)	$r$ (kpc)	$L_K$ $10^{11} L_\odot$	$M_{\text{gas}}$ $10^{11} M_\odot$	IMLR	OMLR	MMLR
					$\times 10^{-4} (M_\odot/L_\odot)$		
0.025	2	22	1.5	0.084	$0.79^{+0.08}_{-0.07}$	$1.7^{+0.5}_{-0.4}$	$0.50^{+0.06}_{-0.05}$
0.050	4	44	2.0	0.44	$3.3^{+0.3}_{-0.3}$	$9.1^{+2.1}_{-2.0}$	$2.1^{+0.2}_{-0.2}$
0.076	6	66	2.1	1.0	$5.8^{+0.5}_{-0.4}$	$13^{+4}_{-4}$	$3.6^{+0.4}_{-0.4}$
0.11	9	100	3.1	2.2	$7.3^{+0.6}_{-0.6}$	$19^{+6}_{-6}$	$4.6^{+0.6}_{-0.5}$
0.19	15	167	6.4	5.1	$6.3^{+0.5}_{-0.5}$	$20^{+5}_{-5}$	$4.3^{+0.5}_{-0.4}$
0.29	23	256	7.0	9.9	$7.9^{+0.9}_{-0.7}$	$21^{+11}_{-5}$	$5.7^{+0.9}_{-0.6}$
0.10*	7.9	88	3.1	1.7	$6.0^{+0.4}_{-0.4}$	$15^{+4}_{-4}$	$3.8^{+0.4}_{-0.4}$
0.30*	24	264	7.0	1.0	$8.1^{+1.0}_{-0.8}$	$21^{+12}_{-5}$	$5.9^{+0.9}_{-0.7}$

\* To compare with the results of other objects in Figure 14, we recalculated metal mass-to-light ratios at  $r = 0.1 r_{180}$  and  $r = 0.3 r_{180}$

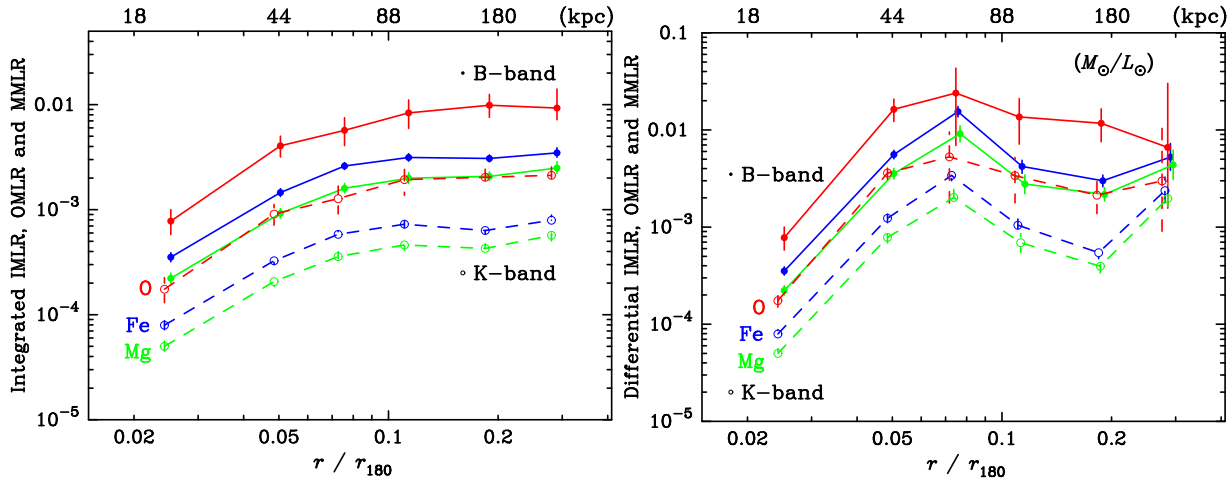


**Fig. 13.** (Left) Radial profiles of integrated IMLR (blue), OMLR (red) and MMLR (green) in B-band (solid lines) and K-band (dashed lines). (Right) Radial profiles of differential mass-to-light ratios with the same representation as in the left panel.

5044 group is lower than those of clusters, but the IMLR is comparable to those of clusters. The metal distribution of the ICM can be used as a tracer of the past history of heating and enrichment in the clusters of galaxies.

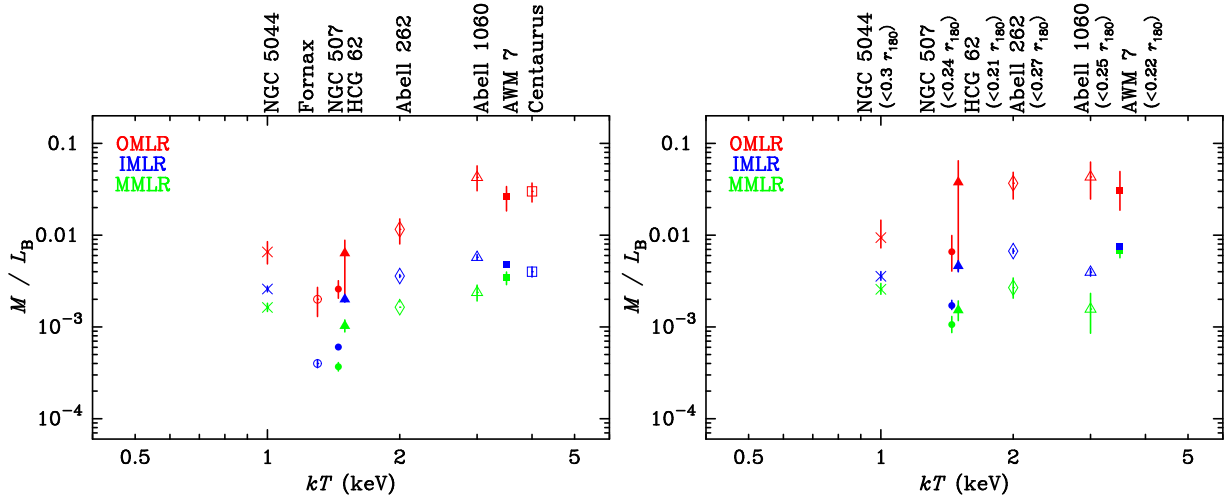
## References

- Anders, E., & Grevesse, N. 1989, *Geochim. Cosmochim. Acta*, 53, 197
- Annibali, F., Bressan, A., Rampazzo, R., Zeilinger, W. W., & Danese, L. 2007, *A&A*, 463, 455
- Betoya-Nonesca, J. G., Fukazawa, Y., & Ohsugi, T. 2006, *PASJ*, 58, 103
- Buote, D. A., Lewis, A. D., Brighenti, F., & Mathews, W. G. 2003, *ApJ*, 594, 741
- Buote, D. A., Lewis, A. D., Brighenti, F., & Mathews, W. G. 2003, *ApJ*, 595, 151
- Buote, D. A., Brighenti, F., & Mathews, W. G. 2004, *ApJL*, 607, L91
- David, L. P., Jones, C., Forman, W., & Daines, S. 1994, *ApJ*, 428, 544
- Evrard, A. E., Metzler, C. A., & Navarro, J. F. 1996, *ApJ*, 469, 494



**Table 7.** Comparison of IMLR, OMLR and MMLR for all systems in B-band (Sato et al. 2008c)

Object	IMLR	OMLR	MMLR	$r/r_{180}$	$k(T)$ (keV)	Reference
Suzaku						
NGC 5044	$2.6^{+0.2}_{-0.2} \times 10^{-3}$	$6.6^{+1.9}_{-1.7} \times 10^{-3}$	$1.6^{+0.2}_{-0.2} \times 10^{-3}$	0.10	$\sim 1.0$	this work
	$3.6^{+0.4}_{-0.3} \times 10^{-3}$	$9.4^{+5.2}_{-2.1} \times 10^{-3}$	$2.6^{+0.4}_{-0.3} \times 10^{-3}$	0.30		
Fornax	$4^{+0.4}_{-0.4} \times 10^{-4}$	$2^{+0.7}_{-0.7} \times 10^{-3}$	-	0.13	$\sim 1.3$	Matsushita et al. (2007a)
NGC 507	$6.0^{+0.4}_{-0.3} \times 10^{-4}$	$2.6^{+0.6}_{-0.5} \times 10^{-3}$	$3.7^{+0.4}_{-0.4} \times 10^{-4}$	0.11	$\sim 1.5$	Sato et al. (2008b)
	$1.7^{+0.2}_{-0.2} \times 10^{-3}$	$6.6^{+3.3}_{-2.5} \times 10^{-3}$	$1.1^{+0.2}_{-0.2} \times 10^{-3}$	0.24		
HCG 62	$2.0^{+0.2}_{-0.1} \times 10^{-3}$	$6.4^{+2.4}_{-4.2} \times 10^{-3}$	$1.0^{+0.2}_{-0.1} \times 10^{-3}$	0.11	$\sim 1.5$	Tokoi et al. (2008)
	$4.6^{+0.7}_{-0.6} \times 10^{-3}$	$3.8^{+2.7}_{-3.4} \times 10^{-2}$	$1.5^{+0.4}_{-0.4} \times 10^{-3}$	0.21		
A 262	$3.6^{+0.1}_{-0.1} \times 10^{-3}$	$1.2^{+0.3}_{-0.4} \times 10^{-2}$	$1.6^{+0.2}_{-0.2} \times 10^{-3}$	0.10	$\sim 2$	Sato et al. (2008c)
	$6.7^{+0.4}_{-0.4} \times 10^{-3}$	$3.7^{+1.2}_{-1.2} \times 10^{-2}$	$2.7^{+0.7}_{-0.6} \times 10^{-3}$	0.27		
A 1060	$5.7^{+0.4}_{-0.4} \times 10^{-3}$	$4.3^{+1.4}_{-1.2} \times 10^{-2}$	$2.4^{+0.5}_{-0.5} \times 10^{-3}$	0.12	$\sim 3$	Sato et al. (2007a)
	$4.0^{+0.4}_{-0.4} \times 10^{-3}$	$4.3^{+2.0}_{-1.8} \times 10^{-2}$	$1.6^{+0.8}_{-0.7} \times 10^{-3}$	0.25		
AWM 7	$4.8^{+0.2}_{-0.2} \times 10^{-3}$	$2.6^{+0.8}_{-0.8} \times 10^{-2}$	$3.4^{+0.5}_{-0.5} \times 10^{-3}$	0.11	$\sim 3.5$	Sato et al. (2008a)
	$7.6^{+0.4}_{-0.3} \times 10^{-3}$	$3.1^{+1.9}_{-1.2} \times 10^{-2}$	$6.7^{+1.1}_{-1.1} \times 10^{-3}$	0.22		
XMM-Newton						
Centaurus	$4^{+0.5}_{-0.5} \times 10^{-3}$	$3^{+0.7}_{-0.7} \times 10^{-2}$	-	0.11	$\sim 4$	Matsushita et al. (2007b)

**Fig. 14.** Integrated IMLR (blue), OMLR (red) and MMLR (green) at **(Left)**  $r = 0.1 r_{180}$  or **(Right)**  $r \sim 0.3 r_{180}$  using the B-band luminosity.

- Ferguson, H. C., & Sandage, A. 1990, AJ, 100, 1
- Finoguenov, A., & Ponman, T. J. 1999, MNRAS, 305, 325
- Finoguenov, A., Ponman, T. J., Osmond, J. P. F., & Zimer, M. 2007, MNRAS, 374, 737
- Fukazawa, Y., Makishima, K., Tamura, T., Nakazawa, K., Ezawa, H., Ikebe, Y., Kikuchi, K., & Ohashi, T. 2000, MNRAS, 313, 21
- Grevesse, N., & Sauval, A. J. 1998, Space Sci. Rev., 85, 161
- Ishisaki, Y., et al. 2007, PASJ, 59, 113
- Iwamoto, K., Brachwitz, F., Nomoto, K., Kishimoto, N., Umeda, H., Hix, W. R., & Thielemann, F.-K. 1999, ApJS, 125, 439
- Kaiser, N. 1991, ApJ, 383, 104
- Kobayashi, C., & Arimoto, N. 1999, ApJ, 527, 573
- Koyama, K. et al. 2007, PASJ, 59, 23
- Lin, Y.-T., & Mohr, J. J. 2004, ApJ, 617, 879
- Lodders, K. et al. 2003, ApJ, 591, 1220
- Lumb, D. H., Warwick, R. S., Page, M., & De Luca, A. 2002, A&A, 389, 93
- Makishima, K., Ezawa, H., Fukuzawa, Y., Honda, H., Ikebe, Y., Kamae, T., Kikuchi, K., Matsushita, K., Nakazawa, K., Ohashi, T., Takahashi, T., Tamura, T. & Xu, H. 2001, PASJ, 53, 401
- Markevitch, M., Forman, W. R., Sarazin, C. L., & Vikhlinin, A. 1998, ApJ, 503, 77
- Matsushita, K., Finoguenov, A., Böhringer, H. 2003, A&A, 401, 443
- Matsushita, K., Fukazawa, Y., Hughes, John P., Kitaguchi, T., Makishima, K., Nakazawa, K., Ohashi, T., Ota, N., Tamura, T., Tozuka, M., Tsuru, T. Go, Urata, Y., Yamasaki, N. Y. 2007, PASJ, 59, 327
- Matsushita, K., Böhringer, H., Takahashi, I., & Ikebe, Y. 2007, A&A, 462, 953
- Matsushita, K. in preperation
- Mellier, Y., & Mathez, G. 1987, A&A, 175, 1
- Mitsuda, K., et al. 2007, PASJ, 59, 1
- Morita, U., Ishisaki, Y., Yamasaki, N. Y., Ota, N., Kawano, N., Fukazawa, Y., & Ohashi, T. 2006, PASJ, 58, 719

- Mulchaey, J. S. 2000, *ARA&A*, 38, 289
- Nagino et al. 2008, submitted to *A&A*
- Nomoto, K., Tominaga, N., Umeda, H., Kobayashi, C., & Maeda, K. 2006, *Nuclear Physics A*, 777, 424
- Paolillo, M., Fabbiano, G., Peres, G., & Kim, D.-W. 2002, *ApJ*, 565, 883
- Ponman, T. J., Cannon, D. B., & Navarro, J. F. 1999, *Nature*, 397, 135
- Ponman, T. J., Sanderson, A. J. R., & Finoguenov, A. 2003, *MNRAS*, 343, 331
- Rasmussen, J., & Ponman, T. J. 2007, *MNRAS*, 380, 1554
- Renzini, A., Ciotti, L., D’Ercole, A., & Pellegrini, S. 1993, *ApJ*, 419, 52
- Sato, K., Yamasaki, N. Y., Ishida, M., Ishisaki, Y., Ohashi, T., Kawahara, H., Kitaguchi, T., Kawaharada, M., Kokubun, M., Makishima, K., Ota, N., Nakazawa, K., Tamura, T., Matsushita, K., Kawano, N., Fukazawa, Y., Hughes, J. P. 2007, *PASJ*, 59, 299
- Sato, K., Tokoi, K., Matsushita, K., Ishisaki, Y., Yamasaki, N. Y., Ishida, M., & Ohashi, T. 2007, *ApJL*, 667, L41
- Sato, K., Matsushita, K., Ishisaki, Y., Sasaki, S., Ohashi, T., Yamasaki, N. Y., & Ishida, M. 2008a, *PASJ*, 60, 333
- Sato, K., Matsushita, K., Ishisaki, Y., Yamasaki, N. Y., Ishida, M., & Ohashi, T. 2008b, *ArXiv e-prints*, 805, arXiv:0805.2771
- Sato, K., Matsushita, K., & Gastaldello, F., submitted to *PASJ*
- Schlegel, D. J., Finkbeiner, D. P., & Davis, M. 1998, *ApJ*, 500, 525
- Scharf, C. A., Zurek, D. R., & Bureau, M. 2005, *ApJ*, 633, 154
- Smith, R. K., Brickhouse, N. S., Liedahl, D. A., & Raymond, J. C. 2001, *ApJL*, 556, L91
- Tamura, T., Kaastra, J. S., Makishima, K., & Takahashi, I. 2003, *A&A*, 399, 497
- Tokoi, K., Sato, K., Ishisaki, Y., Ohashi, T., Yamasaki, N. Y., Nakazawa, K., Matsushita, K., Fukazawa, Y., Hoshino, A., Tamura, T., Egawa, C., Kawano, N., Ota, N., Isobe, N., Kawaharada, M., Awaki, H., & Hughes, J. P. 2008, *PASJ*, 60, 317
- Yoshii, Y., Tsujimoto, T., & Nomoto, K. 1996, *ApJ*, 462, 266